

A Spherical Harmonic Approach for the Determination of HCP Texture from Ultrasound: A Solution to the Inverse Problem

Bo Lan¹, Michael J.S. Lowe², and Fionn P.E. Dunne²

¹Department of Engineering Science, University of Oxford, UK

²Imperial College London, UK

Abstract

A new **spherical convolution approach** has been presented which couples HCP single crystal wave speed (the kernel function) with polycrystal **c-axis pole distribution function** to give the resultant polycrystal wave speed response. The three functions have been expressed as spherical harmonic expansions thus enabling application of the de-convolution **technique** to enable any one of the three to be determined from knowledge of the other two. Hence, the forward problem of determination of polycrystal wave speed from knowledge of single crystal wave speed response and the polycrystal pole distribution has been solved for a broad range of experimentally representative HCP polycrystal textures. The technique provides near-perfect representation of the sensitivity of wave speed to polycrystal texture as well as quantitative prediction of polycrystal wave speed. More importantly, a solution to the inverse problem is presented in which texture, as a **c-axis distribution function**, is determined from knowledge of the kernel function and the polycrystal wave speed response. It has also been explained why it has been widely reported in the literature that only texture coefficients up to 4th degree may be obtained from ultrasonic measurements. Finally, the de-convolution **approach** presented provides the potential for the measurement of polycrystal texture from ultrasonic wave speed measurements.

Keywords: texture, spherical harmonics, ultrasound, HCP polycrystals.

1 Introduction

Hexagonal Close-Packed (HCP) materials, e.g. titanium, zirconium, magnesium and their alloys, are highly anisotropic at the single crystal level [1], so the preferred crystallographic orientation distribution of crystals (also referred to as the *texture*) within an HCP polycrystalline aggregate has profound effects on many of its physical and mechanical properties at the macroscopic or component level, including elastic moduli, Poisson's ratio, strength, ductility, toughness, strain hardening, fracture and many more [2, 3].

The specific orientation of a crystal is described by three Euler angles, so the complete texture information of a polycrystal can be encapsulated by a statistical probability function for the three angles called the orientation distribution function (ODF) [4], which enables graphical presentation of texture and is a useful tool to quantify texture. Pole figures, which illustrate the orientation distribution of reciprocal vector directions in the crystal lattice hence contain only a subset of the full ODF information, are frequently used to represent texture [3]. In addition, Kearns [5] found it convenient for HCP materials in industry to use an even smaller fraction of the ODF information contained in the statistical proportions of c-axes aligned along the respective surface directions of the sample, which are then called Kearns factors.

X-ray diffraction was among the first techniques used to measure the ODF. Each test with specific sample alignment gives the pole figure for a certain reciprocal lattice vector according to Bragg's Law [6], and the solution to the inversion problem of obtaining the complete ODF from a series of tests was given by Roe [4], which marked a milestone for texture detection and ensured the prominence of X-ray diffraction for decades. One major disadvantage of the X-ray diffraction technique, however, is that it is only able to give an average distribution within the tested region without any spatial resolution. This was overcome by the Electron Back Scatter Diffraction (EBSD) technique, which has gained great momentum since the 90s and become the most widely used texture detection method [7]. By interpreting the Kikuchi pattern formed by backscattered electrons from crystal lattices, EBSD can obtain accurate orientations at all testing points [7, 8]. But the scanning process is quite slow so tests are usually confined to a very localized region, and the test samples need extremely careful preparation. Spatially Resolved Acoustic Spectroscopy (SRAS) is an excellent alternative technique which overcomes many of these disadvantages of EBSD at the cost of some loss of resolution. By mapping the surface acoustic waves (SAWs) in different directions it can inversely determine the crystallographic orientations across a large region in almost real time [9, 10].

X-ray and EBSD techniques are both destructive during sample preparation, and the three techniques mentioned above are all surface or near-surface techniques, meaning the textures detected are limited within the surface layers of the sample. Even though other techniques like neutron diffraction and X-ray synchrotron can penetrate a volume up to a certain thickness [11, 12], the energy needed is extremely high, hence the tests can only be conducted in certain sites with limited access and are also very expensive. It is therefore desirable for a non-destructive technique capable of bulk texture measurement to be developed, and given their attractive natural properties [13], bulk ultrasonic waves are the best candidate for this task. The efforts devoted to solve this *inverse* problem (i.e. to extract texture from ultrasonic speed measurements, as opposed to the *forward* problem where texture is known and ultrasound wave speed is measured) can be categorized into making use of two ultrasonic wave properties: attenuation and wave velocity variation.

Attenuation of ultrasonic waves is caused by absorption and scattering, and normally only the latter is utilized in theoretical and experimental analyses given the difficulty of measuring absorption and the fact that scattering is expected to dominate in typical cases of attenuation measurements.

Early attempts to relate wave scattering with grain anisotropy were made by Stanke and Kino [14], who developed a theoretical model to predict the attenuation due to scattering within a single-phased polycrystal with anisotropic grains. But because of the randomness of scattering and the resulting attenuation, measurement of attenuation is not capable of capturing information for texture extraction, and thus is mainly used for other purposes, for example grain size detection. Exemplary efforts in this regard include [15–17]. Relations have been found in titanium alloys between ultrasonic scattering and the presence of macrozones (or micro-textured regions, MTRs) [18, 19], which are colonies or regions with a large number of grains configured with similar crystallographic orientations and affect the fatigue lives of titanium alloy components [20]. This has triggered much related research [19, 21–23]. Compared to attenuation, bulk wave velocity is coupled more closely with polycrystal orientation and offers a more rigorous mathematical relationship between the two to be developed. The commonly followed route is first, establish a mathematical expression for the polycrystal elastic properties using single crystal properties and texture information; second, bridge the texture information with ultrasonic wave velocity by using the direct relationship between elastic properties and wave velocities, and finally, employ the range of known wave velocities with the established relationship and invert the resulting equations to give the texture information. However, the inverse process is not a trivial problem for polycrystals and a robust solution has remained elusive.

Polycrystal elastic properties are often calculated using grain average methods where three assumptions apply. The first by Voigt assumes that strain is constant across the polycrystal hence averaging the stiffness matrix by volume fraction gives the overall stiffness matrix of the polycrystal; Reuss, however, assumed stress to be constant and averaged the compliance to give the resulting polycrystal compliance matrix; Hill concluded that the elastic properties should be the average of the Voigt and Reuss results [24]. Relating texture with polycrystal elastic properties can be done by following Roe’s idea of spherical expansion [4]. Morris [25] employed Voigt’s assumption and expanded both the ODF and the 8th order rotation tensor into spherical harmonics and used the orthogonality of the expansion to eliminate the expansion bases and thereby obtained the polycrystal elastic moduli expressed with single crystal moduli and the ODF coefficients for samples with orthorhombic symmetries. Sayers [26] pushed this idea forward by developing explicit expressions between ODF coefficients and wave velocities in different directions and then applying it to austenitic stainless steel to inversely obtain the coefficients. Backus [27] chose to decompose the elastic tensor instead of the rotation tensor into harmonics, of which the relations were later used by Smith et al [28] to study the azimuthal dependence of Love and Rayleigh waves. A helpful summary of the mathematical basis of these theories related to hexagonal materials is given by Li et al [29].

These approaches laid down the theoretical foundations for the majority of the subsequent studies, especially for texture detection on plate-shaped samples where the texture relations with other wave modes like Rayleigh and Lamb waves can also be utilized [30–32]. For example, Sayers [33] derived the expressions for angular variation of ultrasonic waves in hexagonal materials for non-destructive tests; Hairo [31] combined the texture relations with both Rayleigh surface waves and skimming Lamb wave modes to get the non-zero ODF coefficients and obtained coarse pole figures; Kielczynski et al [32] made use of bulk longitudinal wave, Rayleigh surface wave and Lamb wave modes to obtain five texture coefficients for hexagonal samples with orthorhombic symmetry; Thompson et al. [30] and Dixon et al. [34] used only the Lamb wave dependence of texture coefficients to obtain three 4th-order ODF coefficients for cubic materials. Anderson et al. [35] performed similar studies to extract Kearns factors from hexagonal-grained Zircalloys.

The major disadvantages of these studies are firstly, that most of them are based on the assumption of orthorhombic sample symmetry in order to minimize the numbers of unknown ODF coefficients, and

force others to be zero, which inevitably leads to loss of information in most cases. Second, the use of Rayleigh or Lamb waves which only exist in surface layers or thin plates narrows the applicability of the general method, for bulk texture determination; and finally, the ODF coefficients are complex numbers by definition so that when real spherical harmonic expansion is used, information loss occurs because in all these studies, only one real number is recovered for each of the coefficients.

In a previous paper [36], we presented forward studies for hcp titanium and zirconium alloys using both computational and experimental methods and found a strong relationship between texture and polycrystal wave velocity which supported the possibility to capture texture differences by means of ultrasonic wave speed measurement. The possibility was strengthened by Moreau et al [37], who found good agreement between surface ultrasonic and EBSD texture measurements for a titanium sample with macrozones.

In this paper, a rigorous mathematical description is presented to establish the relationship between polycrystal bulk wave velocity and texture, whose form after performing spherical harmonic expansion can be used to carry out both forward and inverse studies with satisfactory accuracy. The paper is organized so that firstly, the theoretical background to single crystal wave velocity is briefly presented, which is followed by the new theoretical framework using spherical harmonics. The approach is assessed firstly in forward studies in which experimental textures are employed in order to determine, using the methodology presented, the corresponding ultrasonic wave speeds. The speeds so predicted are compared with the wave speeds independently determined using dynamic elastic polycrystal finite element techniques. Finally, the methodology is employed for inverse studies, where the current work is of most significance, in which three-dimensional textures, characterised with predicted ODFs, are determined from knowledge of ultrasonic wave speed distributions and single crystal elasticity properties. The predicted ODFs, shown using pole figures, are compared with the originals used in order to generate the representative ultrasonic wave speed distributions.

2 Background

2.1 HCP c-axis pole distributions

HCP crystals are often simplified to be elastically transversely isotropic, in that they are assumed to be isotropic on the basal plane about the *c*-axis (the normal to basal), while having different (normally larger) modulus along the *c*-axis. Hence ultrasonic wave velocity in an HCP crystal depends only on the angle between the wave propagation direction and the *c*-axis, such that the retrievable information from ultrasonic measurements is potentially the orientation of the *c*-axis, or the orientation distribution of the *c*-axes if a polycrystal is considered.

The orientation of the *c*-axis of an HCP crystal in the polycrystalline sample coordinate system *o-xyz* can be specified by the combination of a polar angle θ and an azimuthal angle ϕ , as shown in Figure 1. Therefore, the **statistical pole distribution** of the *c*-axes of all crystals in the sample can be described by a probability function $q(\theta, \phi)$ which satisfies:

$$\int_0^{2\pi} \int_0^\pi q(\theta, \phi) \sin \theta d\theta d\phi = 1 \quad (1)$$

This definition is similar to the plane-normal distribution obtained in diffracted x-ray measurements defined by Roe [4], and the visualization of this function $q(\theta, \phi)$ (with some changes to the normalization method) is a (0001) pole figure of the polycrystal. The main aim of this paper is to present a methodology for the determination of **the *c*-axis distribution function $q(\theta, \phi)$ of the HCP polycrystal**,

as well as its pole figures, from ultrasonic measurements.

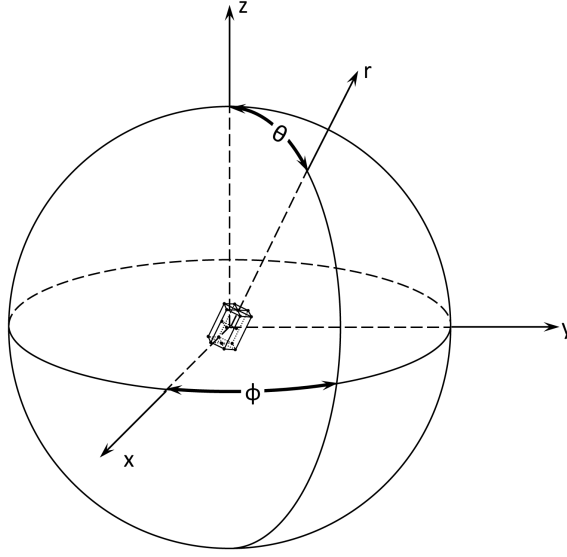


Figure 1: The orientation of an HCP crystal described by two angles

2.2 Single crystal wave velocities

In order to study ultrasonic wave velocity in an HCP crystal, the elastic properties are required. An alpha-phase Ti-6Al-4V single crystal, for instance, has the following stiffness matrix (unit:GPa) when its c-axis lies along the z-axis in an orthogonal coordinate system [38]

$$C = \begin{pmatrix} 170.0 & 92.0 & 70.0 & & & \\ 92.0 & 170.0 & 70.0 & & & \\ 70.0 & 70.0 & 192.0 & & & \\ & & & 39.0 & & \\ & & & & 52.0 & \\ & & & & & 52.0 \end{pmatrix} \quad (2)$$

With knowledge of C_{ijkl} , the ultrasonic wave **phase velocity** in any given direction

$$\mathbf{n} = \begin{pmatrix} \mathbf{n}_1 & \mathbf{n}_2 & \mathbf{n}_3 \end{pmatrix}^T \quad (3)$$

in three-dimensional space can be obtained by solving the well-known Christoffel equation by substituting equations 2 and 3 into those given in Appendix 1 of [36]. It should be noted that our interest in this paper is in the phase velocity of the fastest wave, being the longitudinal wave.

Because the crystal is taken to be isotropic about its c-axis, which is aligned along the z-axis, the velocity on the y-z plane is representative of velocities in all directions. The relationship between θ , which is the incident wave angle defined in Figure 2a and the resulting wave velocity for this particular configuration is shown in Figure 2b. It can be seen that the highest velocity occurs when the wave propagates along the c-axis where $\theta = 0$, and the lowest velocity when the incident wave and crystal c-axis are normal to each other when $\theta = \pi/2$. The response is a periodic function with period of π (not 2π because of the centrosymmetry of ultrasonic tests), and here only a single period, from 0 to

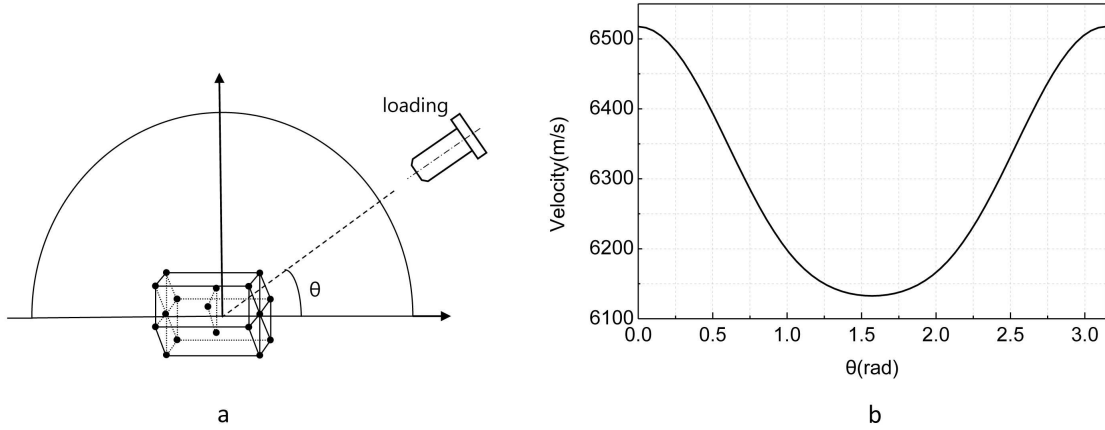


Figure 2: a. An HCP crystal in the reference configuration, and the incident angle θ between the wave direction and the reference direction; b. the compression wave velocity with θ

π , is shown.

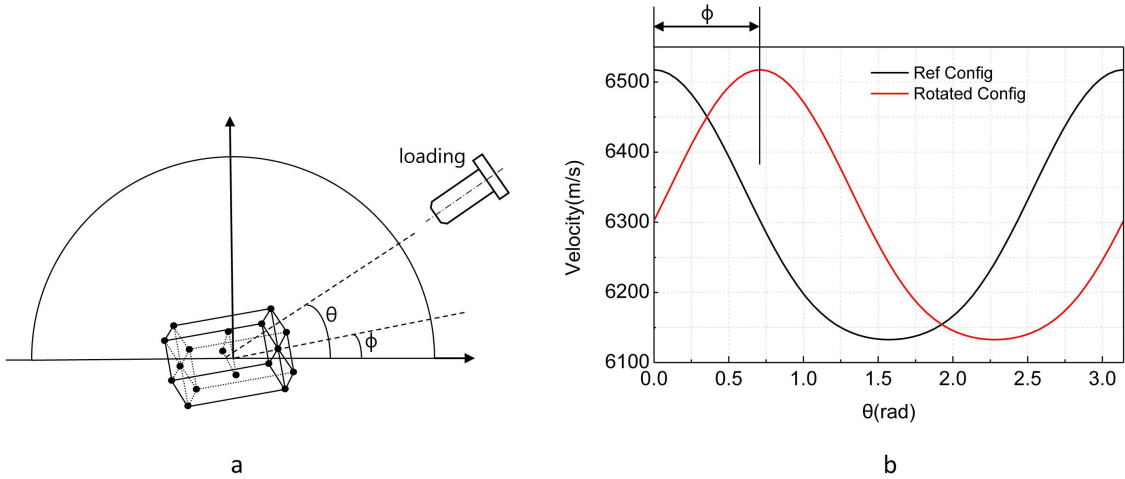


Figure 3: a. An HCP crystal configured with an offset ϕ and the wave incident angle θ ; b. the resulting phase shift caused by ϕ to wave velocity with θ

Next, a crystal which is rotated with an offset angle ϕ from the previous configuration is shown in Figure 3a. The offset introduces only a phase shift with magnitude ϕ so that if the wave velocity response in a single crystal in the reference configuration is $f(\theta)$, then the response of a crystal with orientation ϕ should be $f(\theta - \phi)$, which is shown in Figure 3b, against that for the reference configuration.

3 Theoretical Framework

3.1 Refinement of grain average model

The idea of grain averaging is employed initially to develop the relationships between single crystal orientation, polycrystal texture and polycrystal wave velocity. When incident to an HCP polycrystal from a point source, the wavefront of an ultrasonic wave propagates out approximately in the shape a

sphere; if the wave propagation in a specific direction only is of interest, the problem can be simplified to one dimension in which a wave propagates in a straight line through an array of crystals. Assume that along this particular direction, the volume fraction of crystals with an orientation ϕ_i with respect to the direction is described by $g(\phi_i)$, then the overall velocity in this direction can be calculated by averaging the contribution from grains with differing orientations by:

$$v = \sum f(\phi_i)g(\phi_i) \quad (4)$$

where $f(\phi_i)$ represents the wave velocity through a single crystal with orientation ϕ_i in the specified direction.

Now consider an aggregate of a large number of HCP crystals, with the c-axis of each crystal lying on the same plane, and that the aggregate is statistically homogeneous in such a way that when evaluated from any angle within that plane, the waves go through the same texture. This assumption makes the wave propagation to be a two-dimensional problem. If we define θ as the wave incident angle shown in Figure 3a, then the wave velocity in a crystal with orientation ϕ is $f(\theta - \phi)$. With $g(\phi)$ the volume fraction of crystals with orientation ϕ , the relationship between wave velocity with given direction θ for this two-dimensional case is given by:

$$v(\theta) = \sum f(\theta - \phi_i)g(\phi_i). \quad (5)$$

In polycrystals, crystallographic orientation need not, in fact, remain uniform within a given crystal, or grain. Variations in orientation result from the previous deformation history. Hence, rather than consider a grain-averaged approach, we now allow the possibility that orientation varies continuously such that the summation in equation 5 becomes:

$$v(\theta) = \int_0^\pi f(\theta - \phi)g(\phi)d\phi \quad (6)$$

which is the standard definition of a convolution. It implies that the wave velocity through a two-dimensional aggregate of HCP crystals, where all crystal c-axes remain in-plane, is the convolution between single crystal velocity and the in-plane orientation distribution of crystal point-wise c-axes. In order to generalise into three-dimensional space, two unit direction vectors are introduced such that \mathbf{r}_1 represents the wave propagation direction, and \mathbf{r}_2 the crystal c-axis orientation. Statistical homogeneity remains assumed such that when evaluating the polycrystal from any direction in the space, the ultrasonic waves propagate through the same texture.

A similar integration process as above is adopted with some modification. At a given point in a crystal, the wave velocity depends only on the angle between its propagation direction and the c-axis of the crystal. The wave velocity in direction \mathbf{r}_1 through a crystal with orientation \mathbf{r}_2 is therefore expressed as $f(\arccos(\mathbf{r}_1 \cdot \mathbf{r}_2))$. By definition, \mathbf{r}_1 and \mathbf{r}_2 in three dimensions, considering a point wave source, generate the surface of a unit sphere, so the integration required from equation 6 is written as:

$$v(\mathbf{r}_1) = \int_{\Omega} f(\arccos(\mathbf{r}_1 \cdot \mathbf{r}_2))g(\mathbf{r}_2)d\Omega. \quad (7)$$

Note that \int_{Ω} indicates that the integration is carried out over the whole surface of the unit sphere that \mathbf{r}_2 covers.

Up to now, the function g has been defined as a volume fraction of crystallographic orientation. However, discretising the required summation to infinitesimal units transforms it into an integration and the introduction of \mathbf{r}_2 in equation 7 leads to the same concept as the **c-axis pole distribution func-**

tion $q(\theta, \phi)$ defined in equation 1. If we use q instead of g to denote the distribution, and define a new function k which satisfies $k(\cos(\theta)) = f(\theta)$ to describe the single crystal velocity profile, equation 7 can be re-written as:

$$v(\mathbf{r}_1) = \int_{\Omega} k(\mathbf{r}_1 \cdot \mathbf{r}_2) q(\mathbf{r}_2) d\Omega \quad (8)$$

This expression looks similar to that for classical grain averaging, but the introduction of the two direction vectors for wave direction and crystallographic orientation makes it fundamentally different. In fact, equation 8 is a spherical convolution, and by introducing spherical harmonics, it allows us to perform both forward and inverse studies in relating texture to ultrasonic wave speed.

3.2 Spherical Convolution Theorem

It transpires that many similarities exist between equation 8 and the formulation of a classical problem in computer graphics called radiance and irradiance. In the latter problem, researchers project surrounding light sources onto the reflective surface of a sphere to render a reflection image (or an environment map); or vice versa, try to recover the surrounding light sources from the environment map. An excellent analysis of this problem is presented by Ramamoorthi et al [39, 40], and in the following, we adapt from their approach in order to establish the spherical harmonic theorem for our own study.

3.2.1 Vectors to scalars in the analytical model

For the purpose of convenience, we first transform equation 8 from vector to its corresponding scalar form. A given crystallographic orientation direction of \mathbf{r}_2 on the right-hand side of equation 8 provides a rotated local coordinate system $o-x'y'z'$ with respect to which the ultrasonic wave incident direction \mathbf{r}_1 may be evaluated to give the single crystal velocity $k(\mathbf{r}_1 \cdot \mathbf{r}_2)$ in the \mathbf{r}_1 direction. The rotation of the coordinate system may be described using three Euler angles α, β, γ about the $Z-Y'-Z''$ axes respectively according to Roe's convention [4], as shown in Figure 4. However, the third Euler angle does not have physical significance here because the single crystal elastic properties are assumed to be isotropic about the Z'' axis, and the anisotropy is completely determined by the first two angles. However, for the purposes of completeness, the third rotation angle γ is retained, and the physical non-significance of γ is addressed later. Now that the ultrasonic wave velocity $v(\mathbf{r}_1)$ is dependent on the three Euler angles, we re-write it as $v(\alpha, \beta, \gamma)$.

The wave incident direction \mathbf{r}_1 can be described by the combination of a polar angle θ and an azimuthal angle ϕ in the global coordinate system, but the wave velocity depends only on the relative orientation of \mathbf{r}_1 with respect to \mathbf{r}_2 . In other words, it is the set of polar and azimuthal angles θ' and ϕ' of \mathbf{r}_1 with respect to the rotated crystal coordinate system given by \mathbf{r}_2 that determine the wave velocity. Here (θ', ϕ') can be obtained by rotating the original pair (θ, ϕ) using the Euler angles for rotating the global coordinate system. Following the conventions in quantum mechanics, this rotation can be written to the *active* form as [41]:

$$(\theta', \phi') = R^{(a)}(\alpha, \beta, \gamma) \cdot (\theta, \phi) = R_z^{(a)}(\beta) \cdot R_y^{(a)}(\alpha) \cdot R_z^{(a)}(\gamma) \cdot (\theta, \phi) \quad (9)$$

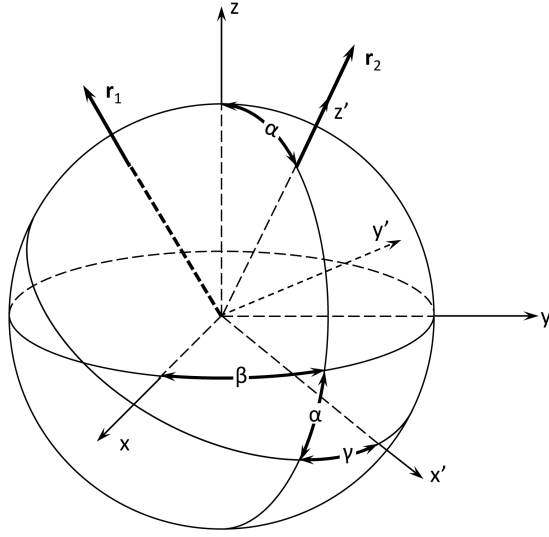


Figure 4: The global coordinate system $o-xyz$ and a rotated local coordinate system $o-x'y'z'$ associated with the crystallographic orientation direction \mathbf{r}_2 . The wave incident direction \mathbf{r}_1 is evaluated with respect to $o-x'y'z'$ to give $k(\mathbf{r}_1 \cdot \mathbf{r}_2)$.

where R_z indicates a rotation about the z axis and similarly, R_y about y axis. The original vector form of equation 8 can now be transformed into the scalar form as follows:

$$\begin{aligned} v(\alpha, \beta, \gamma) &= \int_0^{2\pi} \int_0^\pi k(\theta', \phi') q(\theta, \phi) \sin(\theta) d\theta d\phi \\ &= \int_0^{2\pi} \int_0^\pi k(R^{(a)}(\alpha, \beta, \gamma) \cdot (\theta, \phi)) q(\theta, \phi) \sin(\theta) d\theta d\phi \end{aligned} \quad (10)$$

3.2.2 Spherical Harmonics and their rotations

More subtle properties can be revealed from equation 10 by means of spherical harmonic expansion. Spherical harmonics, which are analogous on the sphere to a Fourier basis on a line or a circle, can be treated as a set of bases upon which any function defined on a sphere can be expanded into harmonic series. The orthogonal spherical harmonic basis of degree l and order m ($-l \leq m \leq l$) is defined as

$$Y_{lm}(\theta, \phi) = P_{lm}(\cos \theta) e^{im\phi} \quad (11)$$

where $P_{lm}(\cos \theta)$ is the *normalized* associate Legendre polynomial which accounts for the effects of the polar angle θ ; while $e^{im\phi}$ means that the dependence of azimuthal angle ϕ in spherical harmonics is described in terms of the Fourier bases. Note that the Condon-Shortley phase is not included in the spherical harmonics used in this paper. We start by expanding $q(\theta, \phi)$ into spherical harmonic (SH) series as similarly carried out by Roe [4]

$$q(\theta, \phi) = \sum_{l=0}^{+\infty} \sum_{m=-l}^l Q_{lm} Y_{lm}(\theta, \phi) \quad (12)$$

where Q_{lm} is the SH coefficient obtained by projecting the original function onto the bases [42]

$$\begin{aligned} Q_{lm} &= \int_{\Omega} q(\theta, \phi) Y_{lm}^*(\theta, \phi) d\Omega \\ &= \int_0^{2\pi} \int_0^{\pi} q(\theta, \phi) Y_{lm}^*(\theta, \phi) \sin(\theta) d\theta d\phi. \end{aligned} \quad (13)$$

Here Y_{lm}^* stands for the complex conjugate of Y_{lm} .

The expansion of the function k in equation 10, however, is more difficult because of the rotations involved. We first expand it in terms of the local angles and SH bases associated with the rotated coordinate system:

$$k(\theta', \phi') = \sum_{n=0}^{+\infty} \sum_{h=-n}^n K_{nh} Y_{nh}(\theta', \phi'). \quad (14)$$

It may be noted that since an HCP crystal is assumed to be elastically isotropic about its c-axis which, under current circumstances, is aligned along the z' -axis, k therefore has no dependence on ϕ' . This symmetry enforces its SH coefficients K_{nh} to be:

$$\begin{aligned} K_{nh} &= \int_0^{2\pi} k(\theta') P_{nh}(\cos \theta') \sin(\theta') d\theta' \int_0^{\pi} e^{ih\phi'} d\phi' \\ &= \begin{cases} K_{n0}, & h = 0 \\ 0, & h \neq 0 \end{cases} \end{aligned} \quad (15)$$

Substituting this relationship back to equation 14 gives:

$$k(\theta', \phi') = \sum_{n=0}^{+\infty} K_{n0} Y_{n0}(\theta', \phi'). \quad (16)$$

By comparing equation 12 and 16, it can be seen that the former expansion is done with respect to global SH bases while the latter to the local crystal system. This difference in the bases is bridged by rotating the global SH bases into the positions of the local ones via the Wigner D-matrix $\tilde{D}^n(\alpha, \beta, \gamma)$ [43]:

$$Y_{n0}(\theta', \phi') = \sum_{m'=-n}^n D_{m'0}^{n*}(\alpha, \beta, \gamma) Y_{nm'}(\theta, \phi) \quad (17)$$

where $D_{m'0}^n(\alpha, \beta, \gamma)$ are elements of the Wigner-D matrix defined as

$$D_{m'0}^n(\alpha, \beta, \gamma) = e^{im'\beta} d_{m'0}^n(\alpha) e^{i0\gamma} = d_{m'0}^n(\alpha) e^{im'\beta}. \quad (18)$$

We follow Ramamoorthi's notation [39] to denote \tilde{D}^n as a $(2n+1) \times (2n+1)$ matrix containing the information about how to describe the rotated SH bases as a linear combination of the original SH bases of the same degree, and $d_{m'0}^n(\alpha)$ in equation 18 are Wigner-d matrix elements directly related to the Jacobi polynomials. Note also that $d_{mn}^l(\alpha)$ follow similar concept with $Z_{lmn}(\cos \alpha)$ defined by Roe in [4], but is not normalized.

Equation 18 shows that the rotations of SH bases do not have any dependence on γ , which follows from the earlier statement about the physical (anisotropic) insignificance of γ . In addition, it can be shown [43] that

$$D_{m'0}^n(\alpha, \beta, \gamma) = \sqrt{\frac{4\pi}{2n+1}} Y_{nm'}(\alpha, \beta) \quad (19)$$

and this property will be utilized as a key point in the following.

3.2.3 The spherical convolution theorem

Now we have gathered all the necessary tools to develop a closed form expression for the convolution relationship in equation 8. Substituting equations 12, 16 and 17 back into 10 leads to the following:

$$\begin{aligned} v(\alpha, \beta, \gamma) &= \int_0^{2\pi} \int_0^\pi k(R^{(a)}(\alpha, \beta, \gamma) \cdot (\theta, \phi)) q(\theta, \phi) \sin(\theta) d\theta d\phi \\ &= \sum_{n=0}^{+\infty} \sum_{m'=-n}^n K_{n0} D_{m'0}^{n*}(\alpha, \beta, \gamma) \sum_{l=0}^{+\infty} \sum_{m=-l}^l Q_{lm} \cdot T_{n,m',l,m} \end{aligned} \quad (20)$$

where:

$$T_{n,m',l,m} = \int_0^{2\pi} \int_0^\pi Y_{nm'}(\theta, \phi) Y_{lm}(\theta, \phi) \sin(\theta) d\theta d\phi = \delta_{l,n} \delta_{m,\bar{m}'}. \quad (21)$$

Where δ represents the Kronecker delta. Because of the orthogonality of spherical harmonics, $T_{n,m',l,m}$ is equal to 1 if and only if $l = n$ and $m' = -m$, which reduces equation 20 into:

$$v(\alpha, \beta, \gamma) = \sum_{l=0}^{+\infty} \sum_{m=-l}^l K_{l0} Q_{lm} D_{-m,0}^{l*}(\alpha, \beta, \gamma). \quad (22)$$

With a few changes of the symbols, equation 19 can be re-written as:

$$D_{\bar{m},0}^{l*}(\alpha, \beta, \gamma) = D_{m,0}^l(\alpha, \beta, \gamma) = \sqrt{\frac{4\pi}{2l+1}} Y_{lm}(\alpha, \beta). \quad (23)$$

Substituting 23 back in to equation 20 and dropping the angle γ on the left side of the equation since wave velocity does not have any dependence on γ simplify the equation to:

$$v(\alpha, \beta) = \sum_{l=0}^{+\infty} \sum_{m=-l}^l \sqrt{\frac{4\pi}{2l+1}} K_{l0} Q_{lm} Y_{lm}(\alpha, \beta) \quad (24)$$

which means that if the velocity v is expanded into an SH series, its SH coefficients are given by:

$$V_{lm} = \sqrt{\frac{4\pi}{2l+1}} \cdot K_{l0} \cdot Q_{lm} \quad (25)$$

and equations 24 and 25 form the spherical convolution theorem for our analysis.

3.3 Discussion of the approach

The relationships between the functions v , k and q are revealed explicitly by the spherical harmonic theorem above, which, firstly, enables us to perform the forward problem where polycrystal wave velocities may be predicted with knowledge of texture; and also, more importantly, provides a solution for the long-standing inverse problem in which texture may be predicted from knowledge of polycrystal wave velocity. Because the single crystal velocities $k(\theta, \phi)$ and their SH coefficients K_{l0} are known, using the convolution theorem from the right side to the left (i.e., convolving the texture SH coefficients with those for the single crystal velocity) to give the polycrystal SH coefficients, and thereby determine polycrystal velocities in different directions, is to perform the forward study. However, if the theorem is used from the left side to the right, i.e., obtain the polycrystal velocities and expand them into

SH coefficients, and then de-convolve the single crystal velocity coefficients from these coefficients to obtain the **c-axis pole distribution SH coefficients**, then that is the inverse problem. Both the forward and inverse problems are examined in the following sections.

In addition, the unique correspondence between the c-axis distribution function q and polycrystal wave speed v in HCP aggregates can now be mathematically demonstrated by the convolution approach. Consider the inverse study for instance. If there are two supposedly different c-axis distributions producing exactly the same polycrystal velocities in all directions, then their SH coefficients V_{lm} must also be identical; and since the kernel coefficients K_{l0} are unique - and so is the pointwise division operation V_{lm}/K_{l0} - the resulting SH coefficients Q_{lm} and function q for the distributions must also be identical, which contradicts with the assumption and thus proves the uniqueness. Similar arguments apply for the forward problem also.

The SH coefficients of functions v , k and q are affected by certain symmetries. For example, ultrasonic wave velocity tests always have centrosymmetry for both polycrystals and single crystals, which means, two waves propagating on the same line but in opposite directions have the same velocity; similarly, two crystals with exactly the opposite orientations are not distinguishable. This implies the relationship

$$v(\theta, \phi) = v(\theta + \pi, \phi + \pi) \quad (26)$$

also holds for k and q . As proved by Roe [4], this symmetry enforces V_{lm} , K_{l0} and Q_{lm} all equal to zero when l is odd.

It should also be noted that even though we are using single crystal phase velocity $k(\theta, \phi)$ as the kernel of the convolution in equation 8, **the model also has the flexibility to change the kernel for other single crystal physical properties that have similar directional variation relationships with k** . For example, the wave slowness, which is defined as a vector along the direction of k with the amplitude of the reciprocal of k and is a crucial concept to Non-Destructive Evaluation (NDE) technology, can also be used as the kernel to calculate phase velocity variations in polycrystals. If single crystal group velocity is used instead of phase velocity k , the outcome of the convolution becomes the variation of group velocity in the polycrystalline aggregate, which is experimentally more easily accessible for some detection techniques such as phased array. Similarly, single crystal Young's modulus can also be used as the kernel to calculate the resultant Young's modulus variations in polycrystals.

4 Forward Studies: Wave Speed from Texture

It has been shown in the previous section that with knowledge of **c-axis pole distribution function $q(\theta, \phi)$** , polycrystal wave velocity SH coefficients can be obtained using the spherical convolution theorem, such that with knowledge of polycrystal texture, wave velocity in any direction in the three-dimensional space can be predicted by constructing the polycrystal wave velocity function $v(\theta, \phi)$ using the ODF and single crystal wave velocity kernel, and their associated SH coefficients. In this section, an example of the forward problem is addressed in detail in which knowledge of polycrystal texture is utilized in order to predict resulting wave speed. We begin with some simple theoretical **c-axis orientation distributions**, and then move on to experimentally representative textures in HCP alloys. Following this, we address in detail multiple examples of the inverse problem in Section 5.

4.1 SH coefficients of single crystal velocities

We start by obtaining the SH coefficients of single crystal velocities. As mentioned in the previous section, the coefficients $K_{lm} = 0$ when $m \neq 0$ because the velocities do not depend on the azimuthal angle; moreover, $K_{l0} = 0$ when l is odd because of the centrosymmetry of the velocities. The corresponding spherical harmonics $Y_{l0}(\theta, \phi)$ for K_{l0} then simplify to $Y_{l0}(\theta, \phi) = P_{l0}(\cos \theta)$, which are *normalized* Legendre polynomials, so the even-degree SH coefficients of single crystal velocities can be obtained by fitting the curve shown in Figure 1b using Legendre polynomials with corresponding degrees. The resulting coefficients decrease with the degree l , and those of *0th* to *8th* degrees are listed in Table 1:

Table 1: SH coefficients of the single crystal velocities

degree l	0	2	4	6	8
K_l^0	22088.30	374.61	58.96	-3.79	-0.29

4.2 Theoretical distributions

The spherical convolution theorem is next utilised for a number of theoretical **pole** distributions in order to obtain predicted velocity profiles. We address a single crystal in its reference orientation, a single crystal in a rotated orientation relative to the incident wave direction, and thirdly, a polycrystal with random texture.

4.2.1 Single Crystal in reference configuration

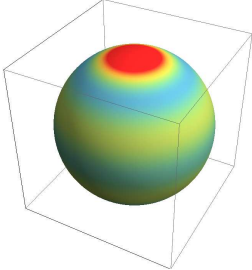
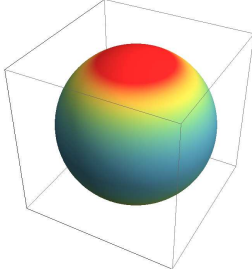
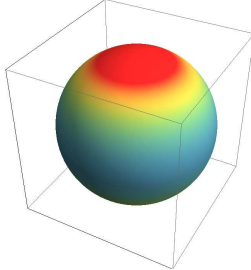
A single crystal clearly satisfies the homogeneity assumption of the analysis such that waves always go through the same texture. The ODF of a single crystal with its *c*-axis oriented in the (θ_0, ϕ_0) direction is a delta impulse at (θ_0, ϕ_0) , hence the SH coefficients are calculated via:

$$Q_{lm} = \int_{\Omega} \delta(\theta_0, \phi_0) Y_{lm}^*(\theta, \phi) d\Omega = Y_{lm}^*(\theta_0, \phi_0) \quad (27)$$

If the single crystal is oriented with reference configuration, i.e., with its *c*-axis along the *z*-axis of the coordinate system, then both θ_0 and ϕ_0 are equal to 0. Hence from equation 27, the SH coefficients Q_{lm} may be obtained and convolved with the kernel coefficients shown in Table 1 using equation 25 to give the coefficients V_{lm} . Based on these SH coefficients, the original velocity, wave speed and orientation functions v , k and q may be computed in all directions with respect to the sample system. For the reference-configured single crystal case, all the *non-zero* SH coefficients of the functions up to 8th degree, along with the spherical visualizations of the functions, are shown in Table 2.

Because the single crystal is oriented in exactly the same configuration with the kernel, the resulting velocity function v should be exactly the same as the kernel velocity function k , and correspond directly with the orientation function (here the single crystal orientation), and this is what is obtained in Table 2.

Table 2: Results for single crystal with reference configuration

OD(q)	Kernel(k)	Velocity(v)
		
$Q_{00} = 1/2\sqrt{\pi}$	$K_{00} = 22088.3$	$V_{00} = 22088.3$
$Q_{20} = \sqrt{\frac{5}{4\pi}}$	$K_{20} = 374.61$	$V_{20} = 374.61$
$Q_{40} = \frac{3}{2\sqrt{\pi}}$	$K_{40} = 58.96$	$V_{40} = 58.96$
$Q_{60} = \sqrt{\frac{13}{4\pi}}$	$K_{60} = -3.79$	$V_{60} = -3.79$
$Q_{80} = \sqrt{\frac{17}{4\pi}}$	$K_{80} = -0.29$	$V_{80} = -0.29$

Figures in this and the following two tables for indicative purpose only.

4.2.2 Single crystal with rotated orientation

Next, consider a single crystal with an orientation rotated away from the reference configuration, say, with $\theta_0 = \pi/4$ and $\phi_0 = \pi/4$. The corresponding SH coefficients are again obtained from equation 27, and the convolution is carried out as before. The resulting SH coefficients up to 4th degree and spherical visualizations are shown in Table 3.

In this example, the resultant velocity function v is expected to maintain the velocity profile of the kernel k , but with the profile rotated in the same way as the pole distribution, q . It is shown in Table 3 that with the appropriate SH coefficients Q_{lm} , the velocity profile obtained after convolution is as expected.

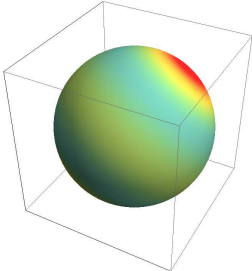
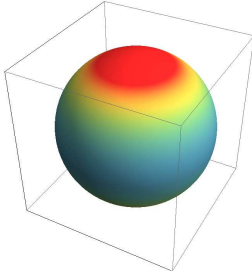
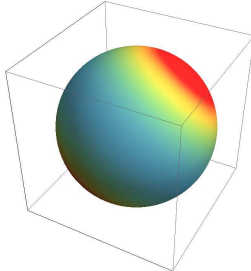
In this example, it may be noted that the SH expansions (shown in Table 3 with up to 4th degree) for both the ODF and the velocity profile contain complex terms. The absence of the inclusion of the full complex form in the ODF distribution would preclude the accurate determination of the resulting velocity profile (as vice versa).

4.2.3 Random orientation

Finally, in this example, the **c-axis pole distribution function** of a theoretically random texture is utilized with the single crystal velocity kernel to investigate the predicted resultant velocity profile. The **pole distribution function** is a constant C over the entire surface of the unit sphere, and from equation 1 it is determined to be $C = 1/4\pi$, such that the SH coefficients are given by:

$$\begin{aligned}
 Q_{lm} &= \int_0^{2\pi} \int_0^\pi \frac{1}{4\pi} \cdot Y_{lm}^*(\theta, \phi) \sin(\theta) d\theta d\phi \\
 &= \frac{1}{4\pi} \int_0^\pi P_{lm}(\cos \theta) \sin \theta d\theta \int_0^{2\pi} e^{im\phi} d\phi
 \end{aligned} \tag{28}$$

Table 3: Results for single crystal with a rotated orientation

OD(q)	Kernel(k)	Velocity(v)
		
$Q_{00} = 1/2\sqrt{\pi}$	$K_{00} = 22088.3$	$V_{00} = 22088.3$
$Q_{20} = 0.1577$		$V_{20} = 93.65$
$Q_{21} = -0.2731 + 0.2731i$	$K_{20} = 374.61$	$V_{21} = -162.21 + 162.21i$
$Q_{22} = -0.1931i$		$V_{21} = -114.70i$
$Q_{40} = -0.3438$		$V_{40} = -23.95$
$Q_{41} = -0.0836 + 0.0836i$		$V_{41} = -5.83 + 5.83i$
$Q_{42} = -0.4182i$	$K_{40} = 58.96$	$V_{42} = -29.13i$
$Q_{43} = 0.2213 + 0.2213i$		$V_{43} = 15.42 + 15.42i$
$Q_{44} = -0.1106$		$V_{44} = -7.71$

Note that only Q_{lm} of order $m > 0$ are shown here, and that $Q_{l\bar{m}} = Q_{lm}^*$ (\bar{m} means $-m$).

which have non-zero values only if both l and m are 0. The convolution process is also performed as before giving the spherical visualization and SH coefficients shown in Table 4.

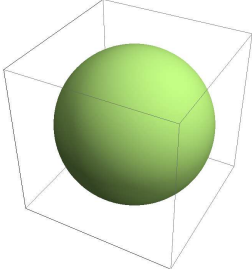
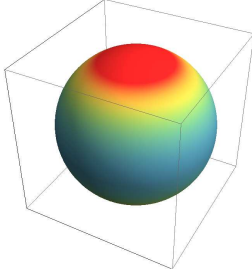
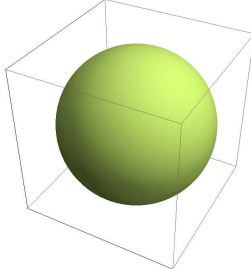
It can be seen in Table 4 that as a result of the random texture, the polycrystal velocities are the same in all the directions, which means the random texture makes the polycrystal elastically isotropic. This property is represented mathematically with all the SH coefficients V_{lm} apart from V_{00} being equal to 0.

4.2.4 Constraints on higher order SH coefficients and truncation errors

The calculation carried out so far for the simple theoretical distributions provide some insights into the nature of the methodology presented for evaluating HCP texture with ultrasonic waves. As listed in Table 1, the SH coefficients of the kernel are found to decrease with degree l , and the 6th and 8th degree coefficients K_6^0 and K_8^0 are -3.79 and -0.29, respectively. Given that the SH coefficients Q_{lm} are always less than or equal to those for the case of the single crystal with reference configuration, it can be shown that the corresponding SH velocity coefficients V_{6m} after convolution always have magnitude less than or equal to 3.79, and V_{8m} in particular is less than 0.29. A consequence of this is that when reconstructing the polycrystal velocities v from the SH coefficients, the impact of texture coefficients of 6th degree is no more than 3.79 m/s; for the 8th degree, no more than 0.29 m/s; and for higher degree, even less.

This leads to two important practical implications. First, when predicting polycrystal velocities using the spherical convolution model with knowledge of the texture SH coefficients, coefficients up to 6th degree are needed to achieve a theoretical velocity accuracy (as opposed to velocities measured

Table 4: Results for random orientation polycrystal

OD(q)	Kernel(k)	Velocity(v)
		
$Q_{00} = 1/2\sqrt{\pi}$	$K_{00} = 22088.3$	$V_{00} = 22088.3$
$Q_{2m} = 0$	$K_{20} = 374.61$	$V_{2m} = 0$
$Q_{4m} = 0$	$K_{40} = 58.96$	$V_{4m} = 0$
$Q_{6m} = 0$	$K_{60} = -3.79$	$V_{6m} = 0$
$Q_{8m} = 0$	$K_{80} = -0.29$	$V_{8m} = 0$

experimentally) of approximately ± 1 m/s. Second and more importantly, when performing inverse studies (see later), since the best accuracy ultrasonic wave velocity tests can possibly achieve is normally worse than ± 3.79 m/s (typically ± 10 m/s), it becomes apparent that it is not possible to recover 6th or higher degree texture SH coefficients from ultrasonic wave velocity tests, because under these circumstances, the introduced numerical noise is already much larger than the SH coefficient information to be extracted. This explains mathematically why it has been widely reported in the literature that only texture coefficients up to 4th degree are obtained [26, 31, 32, 34, 35]. Note that the SH coefficients arising in Tables 1 – 4 relate to HCP Ti-6Al-4V alpha phase, but that in general, the order of SH coefficients theoretically obtainable is determined by the spherical expansion of a given material's single crystal elastic properties.

Since the SH texture coefficients up to 4th degree are the practical goal, **the impacts of the truncation need to be considered. Apart from causing significant intensity changes to the reconstructed function (as will be demonstrated later), it also causes truncation errors.** Two extreme distributions, namely a single crystal and the theoretically random texture, should set the upper and lower bounds of the error respectively in any arbitrary case. A single crystal, whose distribution function is a delta impulse at a given orientation on the unit sphere and whose SH coefficients can be expanded to an infinite degree, leads to the largest truncation error, whose standard deviation is calculated from [4] as:

$$\begin{aligned}
 \delta_q^2 &= \int_0^{2\pi} \int_0^\pi \left(q(\theta, \phi) - \sum_{l=0}^4 \sum_{m=-l}^l Q_{lm} Y_{lm}(\theta, \phi) \right) \sin \theta d\theta d\phi \\
 &= \int_0^{2\pi} \int_0^\pi \sum_{l=6}^{+\infty} \sum_{m=-l}^l Q_{lm} Y_{lm}(\theta, \phi) \sin \theta d\theta d\phi \\
 &\approx \int_0^{2\pi} \int_0^\pi \sum_{l=6}^{N_0} \sum_{m=-l}^l Q_{lm} Y_{lm}(\theta, \phi) \sin \theta d\theta d\phi
 \end{aligned} \tag{29}$$

where N_0 is the order to numerically calculate the error. For EBSD tests N_0 is often chosen as 16, so compared to EBSD tests the standard deviation of the truncation $\delta_q^2 = 10.98$. Note though, that this is the extreme case of orientation distribution, and any real distribution will lead to far less error. For the theoretically random texture, however, the orientation is uniform all over the sphere with only its 0th degree coefficient having a non-zero value, such that truncating the coefficients up to 4th degree does not cause any error at all. Hence, for any arbitrary texture, the standard deviation of the truncation error lies in the range of $[0, 10.98]$, and the stronger the texture approaches a particular orientation, the larger the truncation error. Conversely, the closer the texture is to being random, the smaller the error. Awareness of the existence and origin of these errors may facilitate their diminution, but this has not been addressed in this paper.

4.3 Studies with real example textures

4.3.1 Finite Element model and simulated wave velocities

In a previous paper [36], a Representative Volume Element (RVE) finite element model in Abaqus/Explicit, as shown in Figure 5a, was established in order to simulate the ultrasonic wave propagation in single-phased HCP polycrystals, taking full account of their crystallographic orientations, and hence texture, resulting from the elastic anisotropy. The model was able to accommodate 2160 crystals, with each being assigned an arbitrary orientation, such that a range of differing collective crystallographic textures could be studied, and in particular, the overall ultrasonic wave speeds for the differing textures could be determined **using the simulated transmission wave method**.

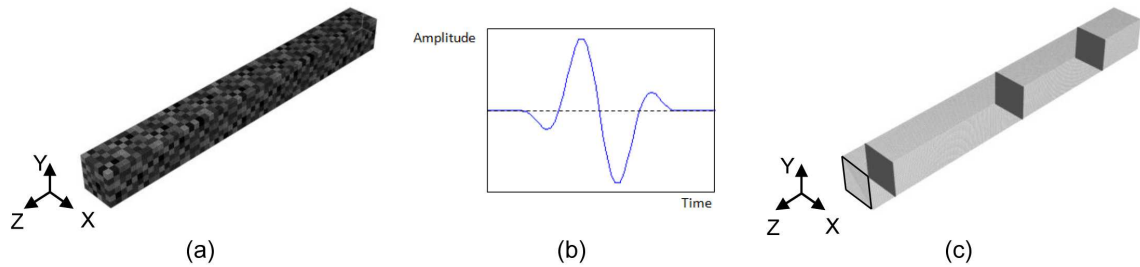


Figure 5: a. The RVE model containing 2160 crystals; b. ultrasonic wave loaded as sinusoidal pulses in Hanning window; c. planes in the model for wave loading and data extraction [36].

The ultrasonic wave signals were induced as pressure waves whose amplitudes are sinusoidal pulses in a Hanning window as shown by Figure 5b [36]. The centre frequency of the pulses is 3MHz, yielding the ratio of wavelength to crystal size at about 10. They were initially applied on the near end of the bar and then propagated along the model through a number of planes (Figure 5c) on which stresses and strains were tracked to determine the respective peak times from which the average wave velocities could be calculated. **It is emphasized that by employing transmission waves, whose speed is expected to be dominated by the overall crystallographic texture (see, for example, [44]), the RVE model takes account of the collective effect of the overall texture only and discards the information of morphology, the arrangements of individual grains and grain boundaries. The relatively negligible effect of the discarded information has been demonstrated via verification of the RVE model by using EBSD texture information from samples which underwent experimental ultrasonic scans, where good agreement was achieved between the computational and experimental results [36].**

Nine differing experimentally representative HCP textures, whose (0001) pole figures are illustrated in Figure 6, were implemented within the RVE model and hence the resulting ultrasonic wave speeds

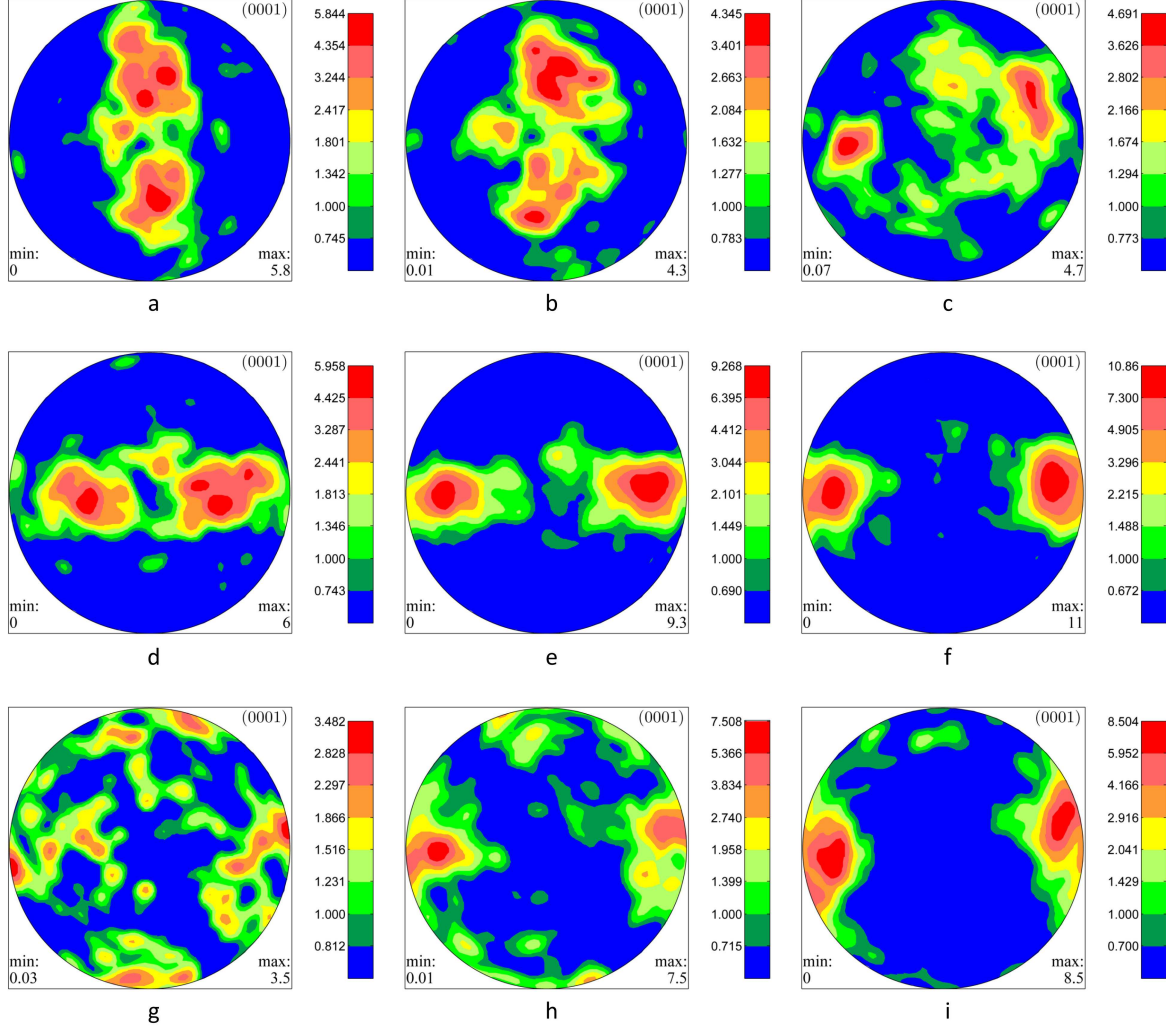


Figure 6: Nine differing experimentally representative pole figures (from Figure 13 in [36] with colour coding changed).

were determined for the respective textures. The wave velocities so obtained are shown in Figure 7 (and labelled as Simulation results). A clear dependence of the wave velocity on the polycrystal texture was observed, and the textures considered included those representative of a reasonably random polycrystal arrangement (eg Figure 6g) through to extremes of very highly textured arrangements (eg Figure 6i), with many intermediate and differing textures. In Figure 7, the wave speeds determined for the range of textures can be seen to be bounded by the two extreme single crystal orientations (labelled SC and SC90 in the figure) with respect to incident wave direction. Included in the figure are also RVE-determined wave speed results for a range of realisations of random polycrystals (labelled Random zone in the figure), indicating the range of wave speed expected for random textures. These independent calculations of wave speed for differing textures are used to compare with the predictions of the current convolution technique in the forward problem.

4.3.2 Convolution studies

We now proceed to performing forward studies on the nine textures using the spherical convolution model. It is firstly necessary to calculate the SH texture coefficients Q_{lm} based on the known textures, for which the Matlab package MTEX [45] is a useful tool. Then, from equation 25, only a few pointwise

multiplications are needed to obtain the polycrystal SH wave velocity coefficients, so that the wave velocity function in three-dimensional space may be reconstructed and hence the wave velocity in any given direction determined. Since in our independent RVE computational studies, only the wave speeds in one direction for each of the textures was examined - that is, along the z -axis in Figure 5c - we now obtain wave velocities from the convolution technique in the corresponding direction only and specify both $\theta = 0$ and $\phi = 0$, in order to draw a straightforward comparison with the computational results. The wave velocities so predicted by the convolution technique are also shown in Figure 7, labelled Velocity. Quantitative numerical comparisons are also listed in Table 5. As discussed before, the convolution technique offers the flexibility to use other physical variables, such as slowness, as the kernel; the details are described in the Appendix, and the wave velocities so determined are also shown in Figure 7 and Table 5 in order to investigate any resulting differences in the context of the textures considered. In addition, for the purpose of demonstrating the comparisons of the convolution technique with the Voigt and Reuss methods, the velocities obtained by respectively averaging stiffness and compliance tensors are also obtained with the help of MTEX [46] and shown in Figure 7 and Table 5.

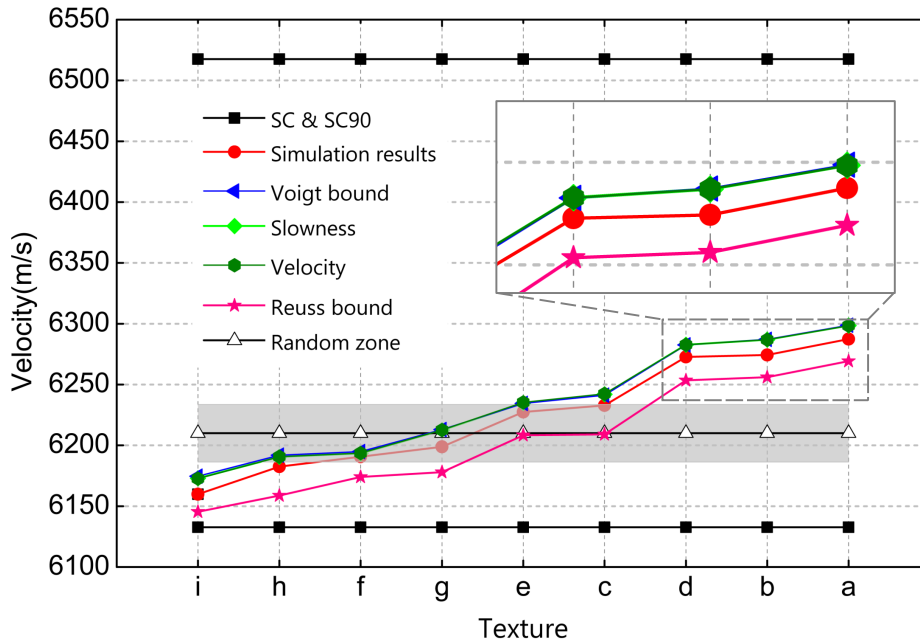


Figure 7: Comparisons between RVE FE [36] and convolution technique wave velocities for the nine textures in Figure 6, with a zoomed-in view at the place marked by the dashed box.

4.3.3 Discussions

Figure 7 shows that the wave velocities predicted by the Voigt and Reuss methods respectively have the largest and smallest magnitudes for a given texture, and the speeds calculated both via the RVE model and by using convolution kernels lie between them, which verifies Hill's conclusion that the Voigt and Reuss methods set up the upper and lower bounds for the polycrystal elastic stiffnesses. The predictions made by using wave velocity and slowness as kernel in the convolution technique are very close, and both kernels capture the changing relationship between polycrystal wave velocity and texture very well. The progressive wave velocity increase with texture sequence predicted by the RVE simulation is also very well captured by the convolution techniques.

Table 5: Comparisons of wave velocities obtained through various methods; row 2 shows simulated results, and rows 3 to 6 are obtained from the convolution method with different kernels (unit: m/s)

Texture	i	h	f	g	e	c	b	d	a
Voigt	6174.6	6191.9	6194.8	6213.0	6234.5	6241.2	6282.6	6287.0	6298.6
RVE FE	6147.1	6164.8	6176.0	6190.0	6221.3	6222.1	6272.4	6273.1	6283.0
Velocity	6172.6	6190.6	6193.6	6212.5	6235.2	6242.3	6282.7	6286.9	6298.4
Slowness	6172.8	6190.6	6193.4	6212.4	6234.9	6241.9	6282.6	6286.9	6298.4
Reuss	6145.4	6158.7	6174.0	6178.0	6208.3	6209.1	6253.3	6255.8	6269.0

It is notable in Figure 7 that the convolution technique, regardless of the kernel used, leads to predicted velocities which are consistently higher than those obtained from the RVE FE simulations and are almost overlapping with those of Voigt’s method. The difference in velocity is typically in the range of 5 ~ 15 m/s. An explanation for this follows from the establishment of the convolution model: it is assumed that the wave propagates as a ray going through a sequence of crystals, without taking any account of the interaction among neighbouring grains. In the RVE FE model, the wave front propagates through the polycrystal, where the crystallographic orientations and resulting elastic anisotropy cause some crystals to result in higher velocity and some lower, along the wave front. This causes local stress fields to form, which influence the average wave speed. Equivalently, because of the crystal anisotropy and the interactions among neighbouring crystals, the individual crystals do not necessarily behave as unstressed single crystals but in fact exhibit subtle differences of elastic properties as a result of the constraint imposed by the continuum requirements of equilibrium and compatibility which are not enforced in the convolution methodology. However, in summary, the convolution technique provides great sensitivity of wave speed to crystallographic texture both qualitatively and quantitatively.

5 Inverse studies: Crystallographic Texture from Wave Speed

A number of forward studies on various theoretical and experimental textures have been successfully performed in the previous section using the spherical convolution model. In this section, we use the spherical convolution model to tackle the long-standing inverse problem; that is, to retrieve polycrystal **c-axis distribution** information from knowledge of spatial ultrasonic wave velocity.

5.1 Discretisation of the problem

For inverse studies of HCP polycrystals, the ultimate objective is the determination of the orientation distribution function of the HCP c-axes, to be reconstructed from its SH coefficients according to the SH expansion theory. The SH texture coefficients may be obtained by de-convolving the single crystal wave velocity from the polycrystal velocity function. Therefore, the first step in extracting the polycrystal texture information from ultrasonic wave speed tests is to establish the polycrystal SH velocity coefficients V_{lm} from experimental results. We wish in this paper to establish proof of principle so that rather than use experimentally measured velocity profiles with which to establish the SH velocity coefficients, we utilize the velocity results obtained from the RVE FE model above.

We then carry out the inverse, or de-convolution process, from these model velocity measurements, in order to re-establish the c-axis distributions from which they were determined. Hence, we aim to predict from the ‘measured’ velocity profiles the c-axis distributions shown by (0001) pole figures in Figure 6.

The SH velocity coefficients V_{lm} are obtained from wave velocity profiles $v(\theta, \phi)$ by projecting v onto the SH basis with degree l and order m which involves the continuous integration over the surface of the unit sphere as follows:

$$V_{lm} = \int_0^{2\pi} \int_0^\pi v(\theta, \phi) Y_{lm}^*(\theta, \phi) \sin(\theta) d\theta d\phi \quad (30)$$

In practice, it is not normally possible to obtain spatially continuous experimental data to perform this integration, and often the best that can be obtained from experiment is a limited set of discrete wave velocity measurements over a given range of incident wave angles on the free surfaces of a typical polycrystal sample. Hence it is often desirable to obtain the SH velocity coefficients from a limited number of discrete test results and this is carried out by means of numerical integration techniques. The general approach for the numerical integration is firstly to discretize the continuous velocity function with a number of nodes and then use the summation of the *weighted* function values at those nodes to approximate the continuous integration. As a result of this approximation, only the accurate coefficients V_{lm} up to a certain degree l_0 can be obtained, hence the original velocity function v becomes band-limited to l_0 when being reconstructed [47, 48]:

$$v(\theta, \phi) = \sum_{l=0}^{l_0} \sum_{m=-l}^l V_{lm} Y_{lm}(\theta, \phi) \quad (31)$$

The degree l_0 achievable depends not only on the number of discrete nodes used, but also on the discretization scheme chosen and the nodal weighting functions used. The latter is often referred to as *quadrature*, and the most widely used methods are equiangular and Gaussian-Legendre quadratures. It was shown by Driscoll and Healy [47] that for a $2N \times 2N$ number of discrete data $f(\theta_i, \phi_j)$ at equiangular grids $\theta_i = \pi i/2N$ and $\phi_j = \pi j/N$ where $i, j = 0, 1, 2, \dots, 2N - 1$, **precision degree of $2N - 1$ for the integrated function (here $f = v(\theta, \phi) Y_{lm}^*(\theta, \phi)$) can be achieved by performing the numerical integration using the following equation:**

$$V_{lm} = \frac{\sqrt{2\pi}}{2N} \sum_{i=0}^{2N-1} \sum_{j=0}^{2N-1} v(\theta_i, \phi_j) Y_{lm}^*(\theta_i, \phi_j) \omega_N(i) \quad (32)$$

where $\omega_N(i)$ is the weight function for the i th node of the polar angle calculated by:

$$\omega_N(i) = \frac{\sqrt{2}}{N} \sin\left(\frac{\pi i}{2N}\right) \sum_{k=0}^{N-1} \frac{1}{2k+1} \sin\left[\frac{(2k+1)\pi i}{2N}\right] \quad (33)$$

It should also be noted that the number N in equations 32 and 33 is restricted to be a power of 2. One of the major disadvantages of the equiangular quadrature scheme, however, is that the number of discrete data needed is rather large. **Taking our problem for example, the desired degree of precision for V_{lm} is 4, which means the degrees of both $v(\theta, \phi)$ and $Y_{lm}^*(\theta, \phi)$ need to be at least 4, so $2N - 1$ must be no less than $2 \times 4 = 8$; and because N has to be a power of 2, the smallest N satisfying these requirements is 8, which means we need 16×16 discrete data to ensure the accuracy.**

The Gaussian-Legendre quadrature, on the other hand, is known for the ability to get to $(2N - 1)$ th

degree of accuracy with $2N \times N$ discrete data [48–51]. The numerical integration is written:

$$V_{lm} = \frac{\pi}{N} \sum_{i=0}^{2N-1} \sum_{j=0}^{N-1} v(\theta_i, \phi_j) Y_{lm}^*(\theta_i, \phi_j) \omega_N(i) \quad (34)$$

where $\omega_N(i)$ is the well-known weight function for the i th Gaussian nodes.

For our problem, since the 4th degree of accuracy is desired, theoretically only 10×5 discrete data are needed, which is much reduced compared to the equiangular quadrature method. Hence, in the following studies, Gaussian-Legendre quadrature is used with $N = 6$ to achieve both accuracy and efficiency.

5.2 Obtaining polycrystal velocities using the RVE model

With the numerical integration method chosen, the next task is to obtain the ultrasonic wave velocities $v(\theta, \phi)$ varying with angles θ and ϕ , which would, in practice, be generated by exciting and detecting ultrasonic waves in different directions through a polycrystal sample of interest which satisfies the underlying assumption of homogeneity. In our study, these velocities are generated using the computational RVE FE model introduced in the previous section. The polycrystal representation is shown in Figure 5a, and we need to obtain wave velocity measurements obtained over a range of incident wave angles.

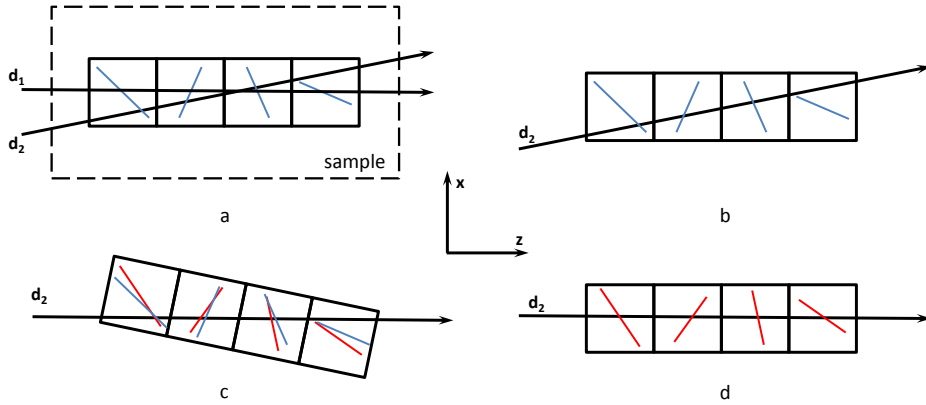


Figure 8: a. The actual testing scheme where the sample remains still and the evaluation direction varies; b. The relative orientations of the crystals to d_2 and the global system; c. The change of crystal orientations with respect to the global system after rotating the whole model to the configuration such that d_2 is along the z -axis; d. The retention of the crystallographic orientations and discarding of the morphology.

The principle of achieving the varying evaluation directions in the RVE model is illustrated in Figure 8. The actual testing scheme is sketched in Figure 8a, where d_1 is along the global z -axis and d_2 along an arbitrary direction, and the blue lines in the boxes represent the c -axis orientations of the crystals. As the wave in the RVE is always applied and propagates along the z -axis, the evaluation in d_2 may be simulated by rotating the whole model in Figure 8b to the required configuration such that d_2 is parallel with z . As a result, the orientations of the crystals are also rotated accordingly with respect to the global coordinate system, as shown by the red lines in Figure 8c opposed to the blue ones, but their relative orientations to d_2 remain unchanged. Next, as shown by Figure 8d, the rotated orientations are retained and input into the RVE model, which ensures that the waves in d_2 go through the same collective crystallographic texture as d_1 ; and the rotated crystal morphologies

are again discarded, as is the case in the un-rotated model in the first instance. Figure 8 illustrates the idea in two dimensions, but it applies to the three dimensional case too, where the orientation of every crystal in the model is subject to the same additional rotation to the configuration corresponding to the desired evaluation direction denoted by θ and ϕ . That is to say that if the sample is associated with a sample system $o-xyz$ and the wave excitation direction with a rotated system $o-x'y'z'$, then evaluating the wave velocity with respect to $o-xyz$ is equivalent to always evaluating the velocity in $o-x'y'z'$ coordinate system with all crystals rotated to its configuration given by $-\theta$ and $-\phi$. This may be achieved using the following rotation matrix applied to each crystal in the aggregate:

$$R = \begin{pmatrix} \cos \theta \cos \phi & -\cos \theta \sin \phi & \sin \theta \\ \sin \phi & \cos \phi & 0 \\ -\sin \theta \cos \phi & \sin \theta \sin \phi & \cos \theta \end{pmatrix} \quad (35)$$

5.3 Results from the convolution model

The nine progressively changing model experimental textures shown in Figure 6 are the subject of our inverse studies. The first step is to obtain the velocity variations with polar and azimuthal angles $v(\theta_i, \phi_j)$ which correspond to each of these textures. Hence, for each texture, 12×6 velocities at the corresponding Gaussian-Legendre grids are simulated using the FE RVE model with configurations specified by equation 35. The SH coefficients of the polycrystal velocities are calculated from the velocity variations based on the numerical integration given by equation 34; then the texture SH coefficients are obtained by de-convolving the single crystal properties from those of the polycrystal through a pointwise division based on the spherical convolution theorem in equation 25. Finally, the **c-axis** distribution of the polycrystal is reconstructed using the SH texture coefficients from which pole intensities in any required orientation may be obtained. The resulting predicted **SH coefficients and pole figure for the texture a** in Figure 6 are detailed in Table 6, and the **predicted pole figures for all the nine textures given in Figure 6 obtained using the computational velocity data and the de-convolution technique** are shown in Figure 9.

Note however, that the normalization convention of the SH coefficients used in reconstructions of the pole figures is different to that defined by equations 1 and 12 and is actually given by:

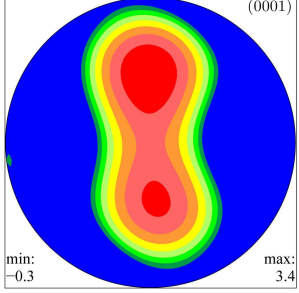
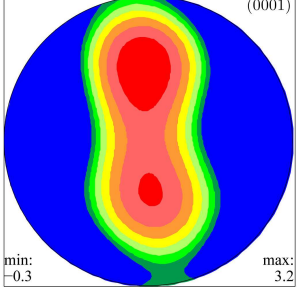
$$Q_{lm}(plot) = 2\sqrt{\pi} \cdot Q_{lm}. \quad (36)$$

This is carried out to ensure that the pole figure density is equal to 1 when the orientation distribution is random [52].

5.4 Discussions

Nine representative HCP textures quantified by **pole distribution functions**, for which (0001) pole figures are shown in Figure 6, have been implemented into an RVE finite element model subjected to simulated ultrasonic wave excitation and the resulting wave velocity dependence on incident wave direction determined. These data are representative of experimental ultrasonic measurements of wave velocity, and have been taken as **the starting point** for proof of principle of determination of **HCP texture ((0001) pole figures or the c-axis distributions)** from knowledge of ultrasonic velocity profiles. The velocity data have been expressed as a spherical harmonic expansion together with that for the single crystal velocity response (the kernel function). The de-convolution technique presented above has then been utilized to extract out the spherical harmonic expansion, and corresponding function

Table 6: SH coefficients and pole figures for texture **a** in Figure 6: original ones and ones determined using the de-convolution technique

Original textures (truncated to 4th degree)	Predicted by de-convolution
	
$Q_{00} = 0.2821$	$Q_{00} = 0.2815$
$Q_{20} = 0.18025$	$Q_{20} = 0.17309$
$Q_{21} = 0.02376 - 0.00320i$	$Q_{21} = 0.02057 - 0.00294i$
$Q_{22} = 0.08062 + 0.01204i$	$Q_{22} = 0.08593 + 0.01165i$
$Q_{40} = -0.00261$	$Q_{40} = 0.00171$
$Q_{41} = -0.00642 + 0.00100i$	$Q_{41} = -0.01163 + 0.00991i$
$Q_{42} = 0.10450 + 0.00821i$	$Q_{42} = 0.08279 + 0.00856i$
$Q_{43} = 0.01641 - 0.01143i$	$Q_{43} = 0.02870 + 0.00507i$
$Q_{44} = 0.03506 + 0.02266i$	$Q_{44} = 0.04192 + 0.02338i$

coefficients, up to order four, for the **c-axis distribution function**, as listed in Table 6, along with those for the original distribution input to the RVE model. It is evident that the SH coefficients are retrieved with reasonably good numerical accuracy; some, for example Q_{40} , are not well recovered only because the original coefficients are too small, hence have minimal impact on the polycrystal wave speed (and on the reconstructed pole figure too). It also needs to be noted that as a result of the recovered coefficients being truncated up to 4th degree only, the intensities in the reconstructed pole figures are not directly comparable to those in the EBSD figures, which are normally truncated to 16th or even 32th degrees. However, if the original EBSD texture is also truncated to 4th degree, as shown in Table 6, it can be seen that the pole figure is in fact very well recovered from the wave velocities.

The recovered c-axis distribution function has then enabled the (0001) pole figures to be shown graphically in Figure 9, such that comparisons between the original pole figures in Figure 6 and those predicted from the de-convolution of velocity profiles may be drawn. From the two figures, it can be seen that the predicted pole figures lack some of the detail, and sharpness, of the originals, but nonetheless provide very substantively the texture information sought, and this has been established over a broad range of differing HCP textures. It is again apparent that for strongly preferred distributions, the magnitude of the intensity drops considerably; in addition, for some of the predicted pole figures, it may be seen that the smallest intensity is less than zero, and the stronger the texture, the bigger the magnitude. Both phenomena are likely caused predominantly by the truncation of the SH

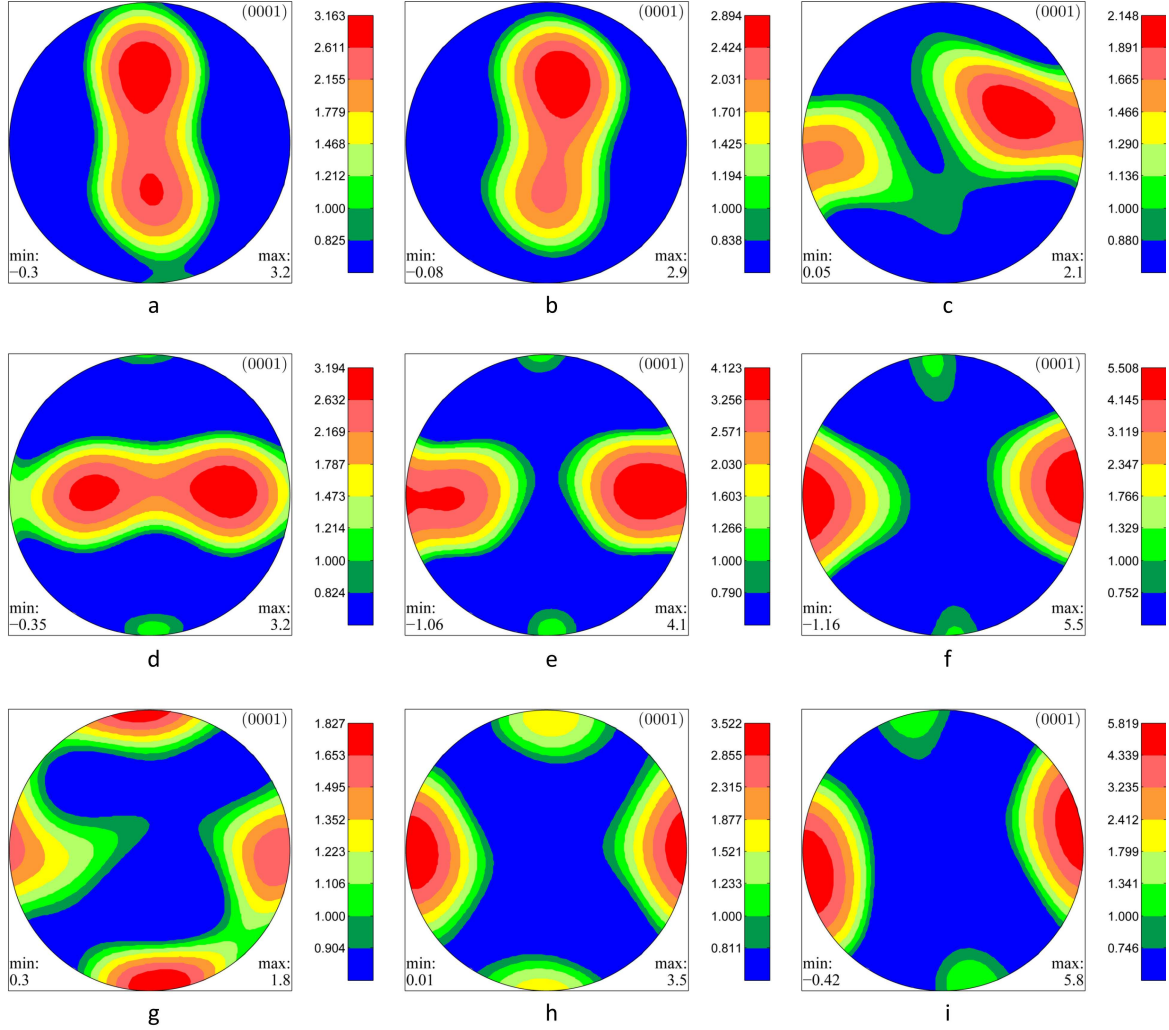


Figure 9: The pole figures predicted from the de-convolution technique for the differing representative experimental textures.

coefficients, coupled with the crystal to crystal interactions which are ignored in the de-convolution technique. In its own right, however, the combination of both magnitudes in each figure is useful in the sense of being indicative of the original intensities, given that those magnitudes for the extreme cases (random texture and single crystals) are easily calculatable and those for a range of differing textures have already been established, which suggests that it is possible to mathematically re-scale the intensities to match the original, un-truncated ones.

The de-convolution technique presented therefore provides a solution to the well-known inverse problem in texture, and significant efforts towards proof of principle has been accomplished so that full three-dimensional, bulk texture measurements may be made in HCP polycrystals from ultrasonic wave velocity measurements. The current work has utilized simulation-generated wave velocity profiles to demonstrate proof of principle. However, the direct experimental measurement of ultrasonic wave velocity is now well established and current techniques include the phased-array [53] approach in which an array of transducers is employed both to emit and receive ultrasonic signals over an area, for example, facilitating the provision of ultrasonic wave speeds in many directions within the material, precisely as required by our de-convolution technique. Naturally, the same requirements for statistically homogeneous texture within the bulk of the polycrystal material still hold, but it is to

be hoped that, through definition of an appropriately sized volume, the spatial variations of texture may now be explored using ultrasonic techniques combined with de-convolution. The prospect for three-dimensional bulk component measurement of texture is therefore much closer.

6 Conclusions

A new convolution approach which couples single HCP crystal wave velocity (the kernel function) response to incident wave angle with the c-axis pole distribution function in order to provide the polycrystal velocity response has been established. The kernel function, c-axis distribution function and polycrystal wave velocity response are represented using spherical harmonic expansions therefore providing full three-dimensional spherical characterisation of all three functions, and importantly, the potential for de-convolution when knowledge of two out of the three functions is known.

In the forward problem, the convolution technique has been shown to allow polycrystal wave speed to be determined from knowledge of the polycrystal orientation distribution and the single crystal wave speed response (and other kernels) to orientation. The polycrystal wave speeds were predicted for a broad range of nine representative experimental single-phase HCP textures showing perfect sensitivity of wave speed to texture and quantitatively good agreement with wave velocity.

It has been demonstrated that the technique allows for de-convolution to be carried out so that with knowledge of the single crystal wave speed response to orientation, and the polycrystal wave speed response, it is now possible to de-convolve the underlying crystallographic pole distribution up to degree four in the **pole distribution function** spherical harmonic expansion. The de-convolution process has been demonstrated for the nine representative HCP polycrystal textures for which knowledge of their wave velocity responses, together with the underlying single-crystal wave response, has been employed to extract out the polycrystal c-axis pole distribution function. The pole figures predicted in this way have been compared with the original polycrystal pole figures from which the wave velocity profiles were obtained, showing very good quantitative agreement. It has been demonstrated that the order of the spherical harmonic expansion of the kernel function – here the single crystal wave velocity response to wave incident angle – explains why it has been widely reported in the literature that only texture coefficients up to 4th degree may be obtained from ultrasonic measurements.

Convolution kernels of velocity and slowness give polycrystal wave speeds which lie between the Voigt and Reuss methods which verifies Hill's conclusion that the latter methods set up the upper and lower bounds for the polycrystal elastic stiffnesses.

Finally, **significant efforts towards proof of principle has been accomplished so** that texture measurement may be made for HCP polycrystals from knowledge of their **(simulated)** ultrasonic wave speed response to orientation, **and experimental validations will be the major follow-ons for further validations of the method.**

Acknowledgement

The authors would like to thank Prof. Tony Wilson of Oxford University and Dr. Peter Huthwaite of Imperial College London for inspiring discussions at the beginning of the work, Dr. Ben Britton for help provided in developing codes for plotting pole figures, and Mr. Pawel Palczynski for helpful discussions of the literature.

Appendix A Convolution using slowness as the kernel

With the phase velocities for an HCP material calculated, it is easy to obtain the relationship of slowness changing with any given direction in the three-dimensional space; and then the SH coefficients can be obtained by performing spherical harmonic expansion on the results, as listed in Table A.1. Note that only the coefficients up to the 6th degree are listed since they are the only ones needed to achieve a desirable accuracy, as explained in Section 4.2.4.

Table A.1: SH coefficients slowness of the single crystal of Ti-6Al-4V

degree l	0	2	4	6
Slowness($\times 10^{-6}$)	160.5	-6.046	-1.177	0.1376

After the polycrystal slowness function s is obtained from using single crystal slowness as the kernel and convolving with the c-axis distribution, the wave velocity $v(\theta, \phi)$ can then be calculated by:

$$v(\theta, \phi) = \frac{1}{s(\theta, \phi)}. \quad (\text{A.1})$$

References

- [1] Gerd Lutjering and James Case Williams. *Titanium*, volume 2. Springer, 2003.
- [2] Y. N. Wang and J. C. Huang. Texture analysis in hexagonal materials. *Materials Chemistry and Physics*, 81(1):11–26, 2003.
- [3] U. Fred Kocks, Carlos Norberto Tome, and H. R. Wenk. *Texture and anisotropy: preferred orientations in polycrystals and their effect on materials properties*. Cambridge university press, 2000.
- [4] R. J. Roe. Description of crystallite orientation in polycrystalline materials .3. general solution to pole figure inversion. *Journal of Applied Physics*, 36(6):2024–2031, 1965.
- [5] J.J. Kearns. Thermal expansion and preferred orientation in zircaloy (lwdr development program). Report, Westinghouse, 1965.
- [6] Bertram Eugene Warren. *X-ray Diffraction*. Courier Dover Publications, 1969.
- [7] Adam J Schwartz, Mukul Kumar, Brent L Adams, and David P Field. *Electron backscatter diffraction in materials science*. Springer, 2009.
- [8] Angus J. Wilkinson and T. Ben Britton. Strains, planes, and ebsd in materials science. *Materials Today*, 15(9):366–376, 2012.
- [9] M. Clark, S. D. Sharples, and M. G. Somekh. Fast, all-optical rayleigh wave microscope: Imaging on isotropic and anisotropic materials. *Ieee Transactions on Ultrasonics Ferroelectrics and Frequency Control*, 47(1):65–74, 2000.

- [10] Steve D. Sharples, Matthew Clark, and Mike G. Somekh. Spatially resolved acoustic spectroscopy for fast noncontact imaging of material microstructure. *Optics Express*, 14(22):10435–10440, 2006.
- [11] Philip John Withers. Depth capabilities of neutron and synchrotron diffraction strain measurement instruments. i. the maximum feasible path length. *Journal of Applied Crystallography*, 37(4):596–606, Aug 2004.
- [12] Philip Withers. Depth capabilities of neutron and synchrotron diffraction strain measurement instruments. ii. practical implications. *Journal of Applied Crystallography*, 37(4):607–612, 2004.
- [13] Jan Achenbach. *Wave propagation in elastic solids*. Elsevier, 1984.
- [14] F. E. Stanke and G. S. Kino. A unified theory for elastic wave-propagation in polycrystalline materials. *Journal of the Acoustical Society of America*, 75(3):665–681, 1984.
- [15] R. Klinman, G. R. Webster, F. J. Marsh, and E. T. Stephenson. Ultrasonic prediction of grain size, strength, and toughness in plain carbon steel. In *Ultrasonic Materials Characterization*, volume 596, page 83. US Department of Commerce, National Bureau of Standards, 1980.
- [16] Jafar Saniee and Nihat M. Bilgutay. Quantitative grain size evaluation using ultrasonic backscattered echoes. *The Journal of the Acoustical Society of America*, 80(6):1816–1824, 1986.
- [17] James H. Rose. Ultrasonic backscatter from microstructure. In *Review of Progress in Quantitative Nondestructive Evaluation. Vol. 11B*, volume 11, pages 1677–1684, 1992.
- [18] Y. K. Han and R. B. Thompson. Ultrasonic backscattering in duplex microstructures: Theory and application to titanium alloys. *Metallurgical and Materials Transactions a-Physical Metallurgy and Materials Science*, 28(1):91–104, 1997.
- [19] A. Bhattacharjee, A. L. Pilchak, O. I. Lobkis, J. W. Foltz, S. I. Rokhlin, and J. C. Williams. Correlating ultrasonic attenuation and microtexture in a near-alpha titanium alloy. *Metallurgical and Materials Transactions a-Physical Metallurgy and Materials Science*, 42A(8):2358–2372, 2011.
- [20] Ioannis Bantounas, David Dye, and Trevor C Lindley. The role of microtexture on the faceted fracture morphology in Ti-6Al-4V subjected to high-cycle fatigue. *Acta Materialia*, 58(11):3908–3918, 2010.
- [21] O. I. Lobkis and S. I. Rokhlin. Characterization of polycrystals with elongated duplex microstructure by inversion of ultrasonic backscattering data. *Applied Physics Letters*, 96(16):161905, April 2010.
- [22] L. Yang, J. Li, O. I. Lobkis, and S. I. Rokhlin. Ultrasonic propagation and scattering in duplex microstructures with application to titanium alloys. *Journal of Nondestructive Evaluation*, 31(3):270–283, 2012.
- [23] L. Yang, J. Li, and S. I. Rokhlin. Ultrasonic scattering in polycrystals with orientation clusters of orthorhombic crystallites. *Wave Motion*, 50(8):1283–1302, December 2013.
- [24] R. Hill. The elastic behaviour of a crystalline aggregate. *Proceedings of the Physical Society of London Section A*, 65(389):349–355, 1952.

- [25] P. R. Morris. Averaging fourth-rank tensors with weight functions. *Journal of Applied Physics*, 40(2):447–448, 1969.
- [26] C. M. Sayers. Ultrasonic velocities in anisotropic polycrystalline aggregates. *Journal of Physics D-Applied Physics*, 15(11):2157–2167, 1982.
- [27] G. Backus. A geometrical picture of anisotropic elastic tensors. *Reviews of Geophysics and Space Physics*, 8(3):633–671, 1970.
- [28] Martin L. Smith and F. A. Dahlen. The azimuthal dependence of love and rayleigh wave propagation in a slightly anisotropic medium. *J. Geophys. Res.*, 78(17):3321–3333, June 1973.
- [29] Y. Li and R. B. Thompson. Relations between elastic-constants c_{ij} and texture parameters for hexagonal materials. *Journal of Applied Physics*, 67(5):2663–2665, 1990.
- [30] R.B. Thompson, S.S. Lee, and J.F. Smith. Relative anisotropies of plane waves and guided modes in thin orthorhombic plates: Implication for texture characterization. *Ultrasonics*, 25(3):133 – 137, 1987.
- [31] M. Hirao, K. Aoki, and H. Fukuoka. Texture of polycrystalline metals characterized by ultrasonic velocity-measurements. *Journal of the Acoustical Society of America*, 81(5):1434–1440, 1987.
- [32] P. J. Kielczynski, A. Moreau, and J. F. Bussiere. Determination of texture coefficients in hexagonal polycrystalline aggregates with orthorhombic symmetry using ultrasounds. *Journal of the Acoustical Society of America*, 95(2):813–827, 1994.
- [33] C. M. Sayers. Angular dependent ultrasonic wave velocities in aggregates of hexagonal crystals. *Ultrasonics*, 24(5):289–291, 1986.
- [34] S. Dixon, C. Edwards, and S. B. Palmer. Texture measurements of metal sheets using wideband electromagnetic acoustic transducers. *Journal of Physics D-Applied Physics*, 35(8):816–824, 2002. PII S0022-3727(02)30108-6.
- [35] A. J. Anderson, R. B. Thompson, and C. S. Cook. Ultrasonic measurement of the kearns texture factors in zircaloy, zirconium, and titanium. *Metallurgical and Materials Transactions a-Physical Metallurgy and Materials Science*, 30(8):1981–1988, 1999.
- [36] B. Lan, M. Lowe, and F. P. E. Dunne. Experimental and computational studies of ultrasound wave propagation in hexagonal close-packed polycrystals for texture detection. *Acta Materialia*, 63:107–122, 2014.
- [37] A. Moreau, L. Toubal, P. Bocher, M. Humbert, E. Uta, and N. Gey. Evaluation of macrozone dimensions by ultrasound and ebsd techniques. *Materials Characterization*, 75:115–128, 2013.
- [38] J.L.W. Warwick, J. Coakley, S.L. Raghunathan, R.J. Talling, and D. Dye. Effect of texture on load partitioning in ti-6al-4v. *Acta Materialia*, 60(10):4117 – 4127, 2012.
- [39] R. Ramamoorthi and P. Hanrahan. On the relationship between radiance and irradiance: Determining the illumination from images of a convex lambertian object. *Journal of the Optical Society of America a-Optics Image Science and Vision*, 18(10):2448–2459, 2001.
- [40] R. Ramamoorthi and P. Hanrahan. *An efficient representation for irradiance environment maps*, pages 497–500. Computer Graphics. 2001. SIGGRAPH 2001 AUG 12-17, 2001 LOS ANGELES, CA ACM SIGGRAPH.

- [41] M. A. Morrison and G. A. Parker. A guide to rotations in quantum mechanics. *Australian Journal of Physics*, 40:465, 1987.
- [42] Volker Schonefeld. Spherical harmonics, 2005.
- [43] Morris Edgar Rose. *Elementary theory of angular momentum*. Courier Dover Publications, 1995.
- [44] Xin Zhong, Marcel Frehner, Karsten Kunze, and Alba Zappone. A novel ebsd-based finite-element wave propagation model for investigating seismic anisotropy: Application to finero peridotite, ivrea-verbano zone, northern italy. *Geophysical Research Letters*, pages n/a–n/a, 2014.
- [45] F Bachmann, Ralf Hielscher, and Helmut Schaeben. Texture analysis with mtex–free and open source software toolbox. *Solid State Phenomena*, 160:63–68, 2010.
- [46] David Mainprice, Ralf Hielscher, and Helmut Schaeben. Calculating anisotropic physical properties from texture data using the mtex open-source package. *Geological Society, London, Special Publications*, 360(1):175–192, 2011.
- [47] J. R. Driscoll and D. M. Healy. Computing fourier transforms and convolutions on the 2-sphere. *Advances in Applied Mathematics*, 15(2):202–250, 1994.
- [48] Martin J. Mohlenkamp. A user’s guide to spherical harmonics, 2011.
- [49] Kendall Atkinson. Numerical integration on the sphere. *The Journal of the Australian Mathematical Society. Series B. Applied Mathematics*, 23(03):332–347, 1982.
- [50] JAR Blais and Dean Allen Provins. Spherical harmonic analysis and synthesis for global multiresolution applications. *Journal of Geodesy*, 76(1):29–35, 2002.
- [51] Kendall Atkinson and Weimin Han. *Spherical harmonics and approximations on the unit sphere: an introduction*, volume 2044. Springer, 2012.
- [52] A.D. Rollett. Orientation distribution:definition, discrete forms, examples. University Lecture, 2014.
- [53] Bruce W Drinkwater and Paul D Wilcox. Ultrasonic arrays for non-destructive evaluation: A review. *NDT & E International*, 39(7):525–541, 2006.